Citation for published version:
Zhang, X, Wang, Z & Gursul, I 2016, 'Interaction of multiple vortices over a double delta wing', Aerospace Science and Technology, vol. 48, pp. 291-307. https://doi.org/10.1016/j.ast.2015.11.020

DOI:
10.1016/j.ast.2015.11.020

Publication date:
2016

Document Version
Peer reviewed version

Link to publication

Publisher Rights
CC BY-NC-ND

Published version available via: http://dx.doi.org/10.1016/j.ast.2015.11.020

University of Bath

General rights
Copyright and moral rights for the publications made accessible in the public portal are retained by the authors and/or other copyright owners and it is a condition of accessing publications that users recognise and abide by the legal requirements associated with these rights.

Take down policy
If you believe that this document breaches copyright please contact us providing details, and we will remove access to the work immediately and investigate your claim.

Download date: 13. May. 2019

Interaction of Multiple Vortices over a Double Delta Wing

X. Zhang, Z. Wang and I. Gursul

University of Bath, Bath, BA2 7AY, United Kingdom

Abstract

Interaction of strake and wing vortices over a 70°/50° double delta wing were studied experimentally in a wind tunnel using particle image velocimetry (PIV) measurements. The upstream effect of the wing vortex on the formation of the strake vortex was identified. A dual-vortex structure of the strake vortices was observed before the wing vortex developed. Further downstream, wing and strake vortices rotated around each other slowly initially, and then faster with downstream distance, at an increasing rate with increasing incidence. Prior to vortex breakdown, both wing and strake vortices were found meandering in relatively small regions. The correlation between the instantaneous locations of the vortices increases if the vortices become sufficiently close to each other. The proper orthogonal decomposition (POD) analysis of the instantaneous velocity fields suggested that, for both wing and strake vortices, the most energetic mode was displacement in the first helical mode. The most energetic mode reveals out-of-phase displacements when the vortices are close to each other.

Nomenclature

a_M	=	Vortex meandering amplitude
c	=	Wing root-chord length
Re	=	Reynolds number, $\rho U_\infty c/\mu$
t	=	Wing thickness
U_{std}	=	Standard deviation of velocity fluctuations
U_∞	=	Freestream velocity
s	=	Local semi-span
x	=	Chordwise distance
y	=	Spanwise distance
y_i	=	The coordinate of instantaneous vortex location in the spanwise direction
$\bar{y}$	=	The coordinate of time averaged vortex location in the spanwise direction
z	=	Distance from wing surface in the normal direction in the measurement plane
z_i	=	The coordinate of instantaneous vortex location in the normal direction
$\bar{z}$	=	The coordinate of time averaged vortex location in the normal direction
α	=	Angle of attack
μ	=	Dynamic viscosity
ν	=	Kinematic viscosity
ρ	=	Density
ω	=	Vorticity
Λ	=	Sweep angle
N	=	Number of snapshots
r	=	Distance to the wing centerline
PIV	=	Particle image velocimetry
POD	=	Proper orthogonal decomposition
UAV	=	Unmanned air vehicle

I. Introduction

Leading edge vortices play an important role in the aerodynamics of delta wings. A great deal of effort has been focused on the study of these vortices, vortex breakdown phenomenon, and aerodynamics of delta wings, as summarized in several review articles [1,2]. Gursul [3] has noted the lack of emphasis on the unsteady aspects of these flows. There have been very few studies on multiple vortices over aircraft type configurations. The main characteristics of the flow over aircraft configurations are the existence and interaction of multiple vortices that originate from forebodies, wings, strakes, and canards. These interactions are the most challenging aspect of the simulation of flows around aircraft configurations. A recent example of this is the flow simulations [4] of F-16XL aircraft (NATO AVT-113 research activity), where the inner and outer wing vortices interact. While the inner wing vortex was predicted well, the outboard vortex was not. It is believed that this may be due to the interaction of the two vortices and, in particular, the unsteady aspects of the interaction. Vortex interactions also exist on Unmanned Air Vehicles, such as X47-B. However, little is known about the interactions of these multiple vortices. The main objective of this study is to investigate vortex interactions over generic (and simple) wings, and ultimately to enable control of multiple vortices to improve aerodynamic performance and flight control.

Double delta wings [5] have been studied as generic configurations that have multiple vortices and vortex interactions. The main feature of the flow is the presence of both strake and wing vortices. At low angles of attack the vortices remain separate, whereas for flows at higher angles of attack the two vortices interact, coil-up, merge, and vortex breakdown develops. The interaction process and breakdown of the vortices depend on the angle of attack and leading edge sweep angles of the strake and wing [5,6]. Previous studies showed intensified interactions between strake and wing vortices as angle of attack increased, due to

the increasing sizes and strengths of the vortices. Similar observations were also reported by Gai et al. [7] and Sohn and Chung [8]. Two adjacent co-rotating vortices with unequal strengths revolve around a center located on the connecting line between the two vortices. When the strengths of the two vortices are about the same, they tend to spiral around each other but still maintain their identities until merging occurs. It is known from the two-dimensional simulations and experiments that the merging process strongly depends on the strength of the vortices and the separation distance between them [9]. Vortices of comparable strength undergo a symmetric merger, whereas for large differences in strength, catastrophic merger occurs very rapidly as the weaker vortex is split and wrapped around the dominant vortex [10].

Surprisingly, for the interaction of multiple vortices over delta wings, there are no experimental studies that focus on the unsteady aspects. Turbulence kinetic energy and unsteady flow data could be invaluable for the validation of numerical simulations and various turbulence models. Previous simulations have used the time-averaged velocity or surface pressure for comparison. The study of Boelens et al. [4] showed that unsteady data are needed to improve the predictions. Little is known about the unsteady aspects of the interaction of multiple vortices. However, based on our knowledge of vortices on simple delta wings [3], we may expect vortex meandering, helical mode instability of vortex breakdown, quasi-periodic oscillations of breakdown location, and vortex shedding. Some of these unsteady flow phenomena may play a role in the unsteady interactions of multiple vortices. For example, oscillations of strake vortex breakdown may influence the wing vortex breakdown. Alternatively, unsteady features of the wing vortex (due to vortex meandering or helical mode instability) may influence the unsteadiness of the strake vortex. A coupling between the motions of breakdowns is a strong possibility. Additional complexity arises as the main wing has a lower sweep angle and vortex forms closer to the wing surface

for nonslender wings [11]. This results in strong interactions of the vortex with the surface boundary layer and sometimes in a dual-vortex structure at low angles of attack. These features of the nonslender vortices may also have an effect on the unsteady aspects and the interaction of multiple vortices.

This paper reports an experimental study of the interactions of multiple vortices over a 70°/50° double delta wing with the kink at mid-chord. These sweep angles were chosen because simple delta wings with these sweep angles were extensively studied and reported in the literature. Particle Image Velocimetry (PIV) flow measurements over the double delta wing were conducted in a wind tunnel and compared to the flow over a simple slender delta wing with a sweep angle of 70°. Unsteady aspects such as vortex meandering and dominant flow features were analysed and discussed.

II. Experimental Apparatus and Methods

A. Experimental setup

The experiments were conducted in a closed-loop wind tunnel with a test section of 2.13 × 1.52 × 2.70 m, located in the Department of Mechanical Engineering at the University of Bath. The tunnel has a maximum speed of 50 m/s and a freestream turbulence level of around 0.1% of the freestream velocity. Figure 1 shows the experimental arrangement which includes the layout of the working section and the high-alpha rig. The wing models are attached to the high-alpha rig which allows the angle of attack to be varied with an accuracy of ±0.25 degrees as the wind tunnel is running.

A double delta wing model with sweep angles of Λ =70° and 50° (with the kink at mid-chord, as shown in Figure 2), and a simple slender delta wing model of Λ =70° were tested. Both models had a chord length of c = 354 mm and a thickness-to-chord ratio of t/c =

2.8%. Both models were manufactured from Aluminium sheet and had a 45-deg bevel on leading edges, thus producing a sharp leading edge, and a square trailing edge. The wing models were mounted on the high alpha rig through a sting. The sting was mounted on the pressure surface of the wing models; the suction surface of the wing was flat. The models were painted matt black in order to reduce reflections created from the laser sheet during the Particle Image Velocimetry (PIV) measurements. The maximum blockage for the wind-tunnel models was approximately 1.3% at the maximum angle of attack of $\alpha = 32°$. Experiments were conducted at a constant freestream velocity of $U_\infty = 10$ m/s, giving a Reynolds number ($Re = U_\infty\, c\, /\nu$, where U_∞ is the free-stream velocity and ν is the fluid kinematic viscosity) of $Re = 2.34\times10^5$.

B. Particle Image Velocimetry (PIV) measurements

Velocity measurements at various crossflow planes (x/c = 0.25, 0.375, 0.50, 0.625, 0.75, 0.875, 1.00) over the double delta wing model and the simple slender delta wing model were performed using a TSI 2D particle image velocimetry (PIV) system. For the smallest and largest angles of attack ($\alpha = 4°$ and $\alpha = 32°$), we conducted PIV measurements at four planes only: x/c = 0.25, 0.50, 0.75, 1.00. The flow was seeded with olive oil droplets produced by a TSI model 9307-6 multi-jet atomizer. The mean size of the olive oil droplets was estimated as 1 μm. Illumination of the desired plane was achieved using dual 120 mJ Nd:YAG lasers. The laser sheets (with a thickness of around 2 mm) were placed perpendicular to the freestream through the optical glass floor viewing window of the test section (see Figure 1). The images were captured using a TSI PowerView Plus 12bit CCD camera with a resolution of 2048×2048 pixels from a downstream location shown in Figure 1. The camera was mounted on a camera support that was independent of the working section of the tunnel, therefore there was minimum vibration during image capture. A TSI LaserPulse synchronizer unit was utilized to link the camera and the laser to enable accurate capture for

the two frame cross-correlation analysis. The time interval between two frames of PIV measurements was between 7-25 μs, depending on the crossflow plane. The system was operated at a sampling frequency of 3.75 Hz in the cross-correlation mode. The commercial software package Insight 3G and a Hart cross-correlation algorithm were used to analyse the images. For the image processing, an interrogation window size of 24 x 24 pixels was used and thus producing velocity vectors for further processing. The effective grid size was between 1.0-1.5 mm, depending on the crossflow plane. The estimated uncertainty for velocity measurements was 2% of the freestream velocity U_∞. For each case, sequences of 2000 instantaneous frames were taken, and the time averaged velocity and vorticity fields were calculated.

III. Results and Discussion

A. Time-averaged flow

Time-averaged crossflow vorticity patterns over the double delta wing at various chordwise locations and wing incidences are presented in Figure 3. In this figure, the vorticity is normalized by the local semi-span and the freestream velocity. The reason for this choice is that the vorticity magnitude varies substantially with the chordwise distance. (For example, for a conical vortex, it varies with the inverse of chordwise distance from the apex). Therefore, if a fixed length scale such as chord length is used to nondimensionalize, it becomes difficult to display variations near the trailing-edge. At $\alpha = 4^0$, both strake and wing vortices form near the wing surface. With increasing angle of attack, the strake and wing vortices move away from the wing surface and become stronger. Vortex breakdown of both strake vortex and wing vortex are observed at the trailing edge of the double delta wing at $\alpha = 12^\circ$ (Figure 3c). The onset of vortex breakdown moves upstream as the angle of attack is

increased (Figures 3d-h). It is noted that the strake vortex breaks down first. This observation is different from the case reported in [5] for a 76°/40° double delta wing, where the wing vortex breaks down first. This may be due to the lower sweep angle of the wing and larger difference between the wing and strake sweep angles in [5]. It is clear from Figure 3 that the strake and wing vortices interact and coil-up. When the vortices merge, there is also breakdown (this is best illustrated for $\alpha = 12^0$ and $\alpha = 16^0$ near the trailing-edge).

It is observed that, at $x/c = 0.5$ (kink location of the double delta wing), the vorticity pattern exhibits a 'dual-vortex' structure. This is somewhat surprising, given that the wing vortex has not yet developed at this chordwise location. In order to understand the flow physics behind the 'dual-vortex' structure observed over the double delta wing model and also for comparison, PIV measurements over the simple slender delta wing were conducted at $x/c = 0.5$. Figure 4 presents the time-averaged crossflow vorticity patterns over the double delta wing and the simple delta wing at various angles of attack at the fixed station of $x/c = 0.5$. In this figure and in the rest of the paper, the vorticity is nondimensionalized by the chord length as the comparisons were made for the same cross-flow planes. It can be seen that, up to $\alpha = 28^o$, as wing incidence is increased, the vortices over double delta wing and the leading edge vortex over simple delta wing move away from the wing surface and gain strength (Figures 4a-f). However, at $\alpha = 28^o$ and 32^0 (Figures 4g & h), vortex breakdown of the strake vortex over double delta wing is observed, which results in a dramatic decrease of the vorticity magnitude and the loss of coherent vortical structure. Vortex breakdown is however not observed over the simple delta wing model. For all angles of attack tested, the vortex over the simple delta wing is closer to the wing surface. Even at $\alpha = 4^o$ for the double delta wing, the 'dual-vortex' structure is visible. With increasing angle of attack up to $\alpha = 24^o$, the two vortices move away from the surface while rotating about each other. However, it appears that the two vortices merge immediately as there is only one vortex at $x/c = 0.625$

(see Figure 3). The two vortices observed at x/c =0.5 for up to α = 24º eventually merge at higher wing incidences (Figures 4g & h), and exhibit breakdown. The dual-vortex structure is absent for all incidences for the simple delta wing. The dual-vortex structure as well as the major difference in the location of the vortices between the double delta wing and simple delta wing suggest that the wing vortices over the double delta wing have upstream effect on the formation of the strake vortices.

Returning to the time-averaged flow shown in Figure 3, the early stages of the interaction of the strake and wing vortices (between x/c = 0.625 and 0.75) reveal a relatively small increase in the rotation angle between the two vortices. This is shown more clearly in Figure 5, where the crossflow streamline patterns over the double delta wing at x/c = 0.625 and x/c = 0.75 are presented. The definition of the rotation angle is sketched in this figure. It is noted that the rotation angle does not appear to be sensitive to angle of attack at early stages. Although both vortices move away from the wing surface with increasing angle of attack, the relative positions of the vortices do not vary much with angle of attack. This is different than the co-rotating trailing vortices for which the rotation rate is expected to increase linearly with the strength of the vortices [9]. It is observed that, for all angles of attack tested, the wing vortex is slightly closer to the wing surface at x/c = 0.625. At x/c = 0.75, however, the wing vortex moves away from the wing surface and also becomes closer to the strake vortex. Note that, at α = 28º and x/c = 0.75 (Figure 5f), both vortices have broken down, as evidenced by the vorticity patterns (Figure 3g), and this is also reflected in the streamlines spiralling out from the vortex axis.

With increasing chordwise distance, it appears that the rotation angle increases faster (see Figure 3). Also, the interaction at x/c = 0.875 is more sensitive to angle of attack (see Figure 3). This is best seen by comparing the time-averaged vorticity fields of α = 8º, 12º, 16º, 20°, 24°, and 28° in Figure 6. The wing vortex and strake vortex rapidly rotate around each

other with increasing angle of attack. This faster increase of rotation angle with distance and vortex strength (due to incidence) is similar to the "convective stage" described for the co-rotating trailing vortices [9]. However, a direct comparison is not possible due to the varying strength and separation between the vortices with the chordwise distance as well as the orientation of the vortex filaments over the double delta wing.

B. Unsteady aspects

Figure 7 presents the standard deviation of crossflow velocity fluctuations over the double delta wing at various chordwise locations and wing incidences. It is observed that, for all the angles of attack tested, the peak standard deviation for both strake vortex and wing vortex were located near the vortex centers, suggesting large vortex meandering amplitudes. After the vortex breakdown, velocity fluctuations spread over a larger area, however the maximum standard deviation decreases substantially. With increasing angle of attack, velocity fluctuations occupy a larger area over the wing.

In order to quantify the characteristics of the aforementioned vortex meandering, the instantaneous locations of the wing and strake vortices at various chordwise locations and wing incidences were obtained from the instantaneous PIV images. In this paper, the vortex center was defined as the location of maximum vorticity magnitude in the PIV measurement plane and rounded to the nearest grid point, giving an accuracy of half of the effective grid size, which varies from 0.5 to 0.75 mm. Figure 8 presents an example of the time-averaged crossflow vorticity field, instantaneous vorticity field, and the instantaneous locations of the wing vortex and strake vortex in a crossflow plane (x/c = 0.75) over the double delta wing at $\alpha = 12^{\circ}$. (Spacing of the triangle symbols indicates the spatial resolution of the measurements). Colours represent the probability of the wing or strake vortex at each grid point. It can be seen that both the wing vortex and strake vortex meander in an area with the highest probability located near the centers of the time-averaged vortices (Figure 8a).

Figure 9 presents contours of the probability of instantaneous vortex location over the double delta wing at various chordwise locations. It is observed that, for all the wing incidences tested, prior to vortex breakdown, both strake vortex and wing vortex meander in relatively small regions with high probability concentrations near the time-averaged vortex centers. For example, for α = 12º (Figure 9c) and α = 16º (Figure 9d), the area in which the vortices meander is small with a large maximum probability of 20%. As the vortices develop downstream and vortex breakdown occurs, the meandering is spread over a larger area with smaller maximum probability. Note that Figure 9 also reveals the dual-vortex structure at *x/c* = 0.5 and the corresponding contours of the probability of instantaneous vortex locations.

In order to quantify the magnitude of vortex meandering, vortex meandering amplitudes were calculated as $a_M = \sqrt{\frac{\sum (z_i - \bar{z})^2 + (y_i - \bar{y})^2}{N}}$ from the PIV measurements conducted over both the double delta wing and the simple delta wing, here N is the number of PIV snapshots in the crossflow plane, z_i and $\bar{z}$ are the coordinates of instantaneous and time averaged vortex locations in the normal direction, y_i and $\bar{y}$ are the coordinates of instantaneous and time averaged vortex locations in the spanwise direction. Figure 10 shows the variation of vortex meandering amplitude, a_M/c, as a function of streamwise distance *x/c* for all wing incidences tested. It is seen that, generally, the meandering amplitudes of both wing vortex and strake vortex increase as they develop downstream, but at a faster rate after vortex breakdown. A sharp increase in meandering amplitudes is first observed near the wing trailing edge for α = 12º due to the onset of vortex breakdown, and then propagates upstream with increasing incidence. Note that the meandering amplitude for the leading edge vortex over the simple delta wing at *x/c* = 0.5 was also included in Figure 10, which exhibits comparable meandering amplitude to that of the strake vortex over the double delta wing.

In order to further study the possible interactions between wing vortex and strake vortex, the correlation coefficients between instantaneous vortex locations were calculated for all cases where multiple vortices exist. The correlation coefficients were calculated between r_A and r_B (r_A and r_B are instantaneous distances of vortex A and B to the wing centerline in crossflow plane, defined as $r_A = \sqrt{z_A^2 + y_A^2}$ and $r_B = \sqrt{z_B^2 + y_B^2}$). The correlation coefficient is defined as $\frac{\sum_1^N (r_{Ai} - \overline{r_A})(r_{Bi} - \overline{r_B})}{\sqrt{\sum_1^N (r_{Ai} - \overline{r_A})^2} \sqrt{\sum_1^N (r_{Bi} - \overline{r_B})^2}}$, here N is the number of PIV snapshots in the crossflow plane, r_{Ai} and $\overline{r_A}$ are the instantaneous and mean values of r_A, r_{Bi} and $\overline{r_B}$ are the instantaneous and mean values of r_B. Figure 11 shows the results at x/c = 0.5, 0.625, 0.75 and 0.875. Note that, in Figure 11, the correlation coefficient at x/c = 0.5 was between the vortices of the dual-vortex structure that originated from the strake, whereas the correlation coefficients at other streamwise locations were calculated between the strake vortex and the wing vortex. Figure 11a indicates that the correlation coefficient between the vortices of the 'dual-vortex' structure reached -0.4 at α = 12º, then it gradually dropped to near zero at α = 24º and 28º. It is interesting that, at α = 12º, the two vortices are aligned vertically (see Figure 4). It is also clear that the correlation becomes weaker as vortex breakdown develops. Further downstream at x/c = 0.625 the strake and wing vortices are weakly correlated. Surprisingly, with increasing streamwise distance, there is an increase in the correlation coefficient at intermediate incidences α = 12º and 16º (Figures 11b-d). Figure 3 suggests that this is due to the decreasing distance between the vortices before merging.

C. Proper orthogonal decomposition analysis

The proper orthogonal decomposition (POD) analysis expands a random function as a series of deterministic functions with random coefficients so that it is possible to separate the

deterministic part from the random one [12,13]. The energy of stochastic signal is given by the sum of the eigenvalues such that each eigenvalue taken individually represents the energy contribution of the corresponding deterministic function [14]. In the past, the application of POD has been limited by the lack of sufficient data to perform the decomposition. However, the instantaneous velocity fields attainable with particle image velocimetry (PIV) have become a natural complement to POD. When the decomposition involves a sequence of instantaneous velocity fields (as captured from PIV), the method is termed snapshot POD, which was introduced by Sirovich [15]. Lumley [12] decomposed the velocity fields of turbulent flows as a spatial vectorial function and extracted the most energetic (spatial) eigenfunction representing the eddies of the flow. As far as the applications related to the streamwise vortices are concerned, this analysis technique was used to capture the dynamic flow structure of the leading-edge vortices as well as the vortex-tail interaction by extracting its most energetic eigenmodes [16,17]. The POD analysis was also used recently to study the trailing vortices by Roy and Leweke [18] and del Pino et al. [19]. In the present investigation, POD analysis was performed on the captured PIV data in crossflow planes over the simple and double delta wings. The analysis was performed using commercial software TSI GRAD-POD TOOLBOX, which employs the spatio-temporal data analysis technique proposed by Heiland [20]. For each case, the first four most energetic modes were extracted.

Figure 12 presents the cumulative energy distribution, time-averaged vorticity field and the flow structures of the four most energetic modes in a crossflow plane over the simple delta wing at x/c = 0.5 and $\alpha = 12^0$. It can be observed that the 1st (most energetic) mode exhibited one vortex pair which was centered on the time-averaged leading-edge vortex, representing displacement of the vortex. A similar vortex pair was also observed in the 2nd mode (2nd most energetic) along with visible decompositions of the shear layer. A linear combination of these eigenmodes provides displacements of the vortex cores, which can be

characterized as an azimuthal wavenumber of m = 1. The same first helical mode was identified in the meandering of the trailing vortices [18,19] and inlet (ground) vortices [21]. Higher modes with decreasing energy are also shown in Figure 12, which reveal the displacements of the vortex core in various directions as well as the shear layer vortical structures.

Time-averaged vorticity fields and flow structures of the first (most energetic) mode in a crossflow plane over the double delta wing at x/c = 0.5 for various wing incidences are presented in Figure 13. Note that these are the "dual-vortex" structures of the apex vortex at this plane. It is seen that two pairs of counter rotating vortices were present in the 1st mode, corresponding to the two time-averaged vortices. At $\alpha = 12^0$, both vortex pairs in the 1st mode had dominant movement vertically but in the opposite directions, suggesting out-phase meandering of the two vortices. It is noted that this angle of attack corresponds to the most negative correlation coefficient shown in Figure 11. As the wing incidence is increased to $\alpha = 16^0$ and $\alpha = 20^0$, the meandering direction of the two vortices starts to deviate from the vertical direction. It is interesting that the corresponding correlation coefficient decreases (see Figure 11).

Figure 14 shows the time-averaged vorticity fields and flow structures of the first (most energetic) mode in various downstream crossflow planes over the double delta wing at $\alpha = 12^0$. At all the chordwise locations, both wing vortex and strake vortex exhibit a pair of counter rotating vortices in the 1st mode, although the one for the strake vortex at x/c = 0.875 is less clear due to the vortex breakdown (Figure 14c). Note that, at x/c = 0.625 (Figure 14a), the two vortex pairs have relatively large separation, which may explain very small correlation coefficients (Figure 11). At the most downstream location x/c = 0.875 (Figure 14c), the two vortices are much closer, resulting in increased negative correlation.

IV. Conclusions

An experimental investigation of the interaction of multiple vortices over a 70° /50° double delta wing has been performed in a wind tunnel. Particle image velocimetry measurements in crossflow planes at various chordwise locations and wing incidences were conducted. The results were compared with those obtained over a simple slender delta wing with a sweep angle of 70°. The following conclusions can be drawn:

a) At $x/c = 0.5$ (kink location of the double delta wing) before the wing vortex developed, a dual-vortex structure of the strake vortex was identified. The two vortical structures rotate around each other with increasing angle of attack. The upstream effect of the wing vortex also causes the formation of the vortical structure further away from the wing surface compared to the simple delta wing.

b) Strake and wing vortices move closer to each other with increasing angle of attack, resulting in intensified interaction, merging, and earlier onset of vortex breakdown. Rotation of the vortices around each other with increasing distance and incidence is initially slow, but accelerates towards the trailing-edge.

c) Prior to breakdown, both wing and strake vortices were found meandering in relatively small regions with high probability concentrations at the time-averaged vortex centers. The amplitude of vortex meandering exhibits sharp increase after the onset of vortex breakdown. The correlation between the displacements of the vortex cores increases as the time-averaged vortices become closer to each other. The proper orthogonal decomposition (POD) analysis of the captured PIV velocity data indicates that, for all vortices, the most energetic mode was the first helical mode, representing the displacement of the vortex core. When the vortices are closer to each other, their displacement becomes out-of-phase.

References

[1] Lee, M. and Ho, C.-M., 1990, "Lift Force of Delta Wings", *Applied Mechanics Reviews,* vol. 43, pp. 209-221.

[2] Delery, J.M., 1994, "Aspects of Vortex Breakdown", *Progress in Aerospace Sciences,* vol. 30, pp. 1-59.

[3] Gursul, I., 2005, *Survey Article*: "Review of Unsteady Vortex Flows over Slender Delta Wings", *Journal of Aircraft,* vol. 42, no. 2, pp. 299-319.

[4] Boelens, O.J., Badcock, K.J., Elmilgui, A., Abdol-Hamid, K.S., Massey, S.J., 2009, "Comparison of Measured and Block Structured Simulation Results for the F-16XL Aircraft", *Journal of Aircraft,* vol. 46, no. 2, pp. 377-384.

[5] Verhaagen, N.G., 1995, "A Study of the Vortex Flow over a 76/40-deg Double-Delta Wing", AIAA Paper 95-0650.

[6] Rom, J., 1992. *High angle of attack aerodynamics: subsonic, transonic, and supersonic flows.* Springer-Verlag.

[7] Gai, S.L., Roberts, M., Barker, A., Kleczaj, C. & Riley, A.J., 2004. "Vortex interaction and breakdown over double-delta wings". *Aeronaut J,* vol. 108, pp. 27-34.

[8] Sohn, M.H. & Chung, H.S., 2007, "Effects of Strake Planform Change on Vortex Flow of a Double-Delta Wing", *Journal of Aircraft,* vol. 44, pp. 1842-1848.

[9] Cerretelli, C. and Williamson, C.H.K., 2003, "The physical mechanism for vortex merging", *Journal of Fluid Mechanics,* vol. 475, pp. 41-.

[10] Marles, D. and Gursul, I., 2008, "Effect of an axial jet on vortex merging", *Physics of Fluids,* vol. 20, 047101.

[11] Gursul, I., Gordnier, R., and Visbal, M., 2005, "Unsteady Aerodynamics of Nonslender Delta Wings", *Progress in Aerospace Sciences,* vol. 41, no. 7, pp. 515-557.

[12] Lumley, J.L., 1970. Stochastic Tools in Turbulence. *Applied Mathematics and Mechanics,* Vol. 12, Academic Press.

[13] Hinze, J.O., 1975. *Turbulence.* Second edition ed. McGraw Hill, New York.

[14] Berkooz, Z., Holmes, P. and Lumley, J.L. 1993 "The proper orthogonal decomposition in the analysis of turbulent flows", *Annu Rev Fluid Mech*, vol. 25, pp. 539–575.

[15] Sirovich, L., 1987, "Turbulence and the Dynamics of Coherent Structures Parts I–III", *Quarterly of Applied Mathematics,* Vol. 45 (No. 3), pp. 561–590.

[16] Cipolla, K.M., Liakopoulos, A., and Rockwell, D.O. 1998, "Quantitative Imaging in Proper Orthogonal Decomposition of Flow Past a Delta Wing", *AIAA Journal,* vol. 36(7), pp. 1247-1255.

[17] Kim, Y., Rockwell, D. & Liakopoulos, A., 2005, "Vortex Buffeting of Aircraft Tail: Interpretation via Proper Orthogonal Decomposition", *AIAA Journal,* 43(3), pp. 550-559.

[18] Roy, C. & Leweke, T., 2008, "Experiments on vortex meandering", *FAR-Wake Technical Report AST4-CT-2005-012238,* CNRS-IRPHE, also presented in International Workshop on Fundamental Issues related to Aircraft Trailing Wakes.

[19] del Pino, C., Lopez-Alonso, J.M., Parras L. & R., F.-F., 2011, "Dynamics of the wing-tip vortex in the near field of a NACA 0012 airfoil", *The Aeronautical Journal,* vol. 115(No. 1166), pp. 229-239.

[20] Heiland, R.W., 1992. KLTOOL: A Mathematical Tool for Analyzing Spatiotemporal Data. *Arizona State University,* Dept of Mathematics (December).

[21] Wang, Z. and Gursul, I., 2012, "Unsteady characteristics of inlet vortices", *Experiments in Fluids*, vol. 53: 1015-1032.

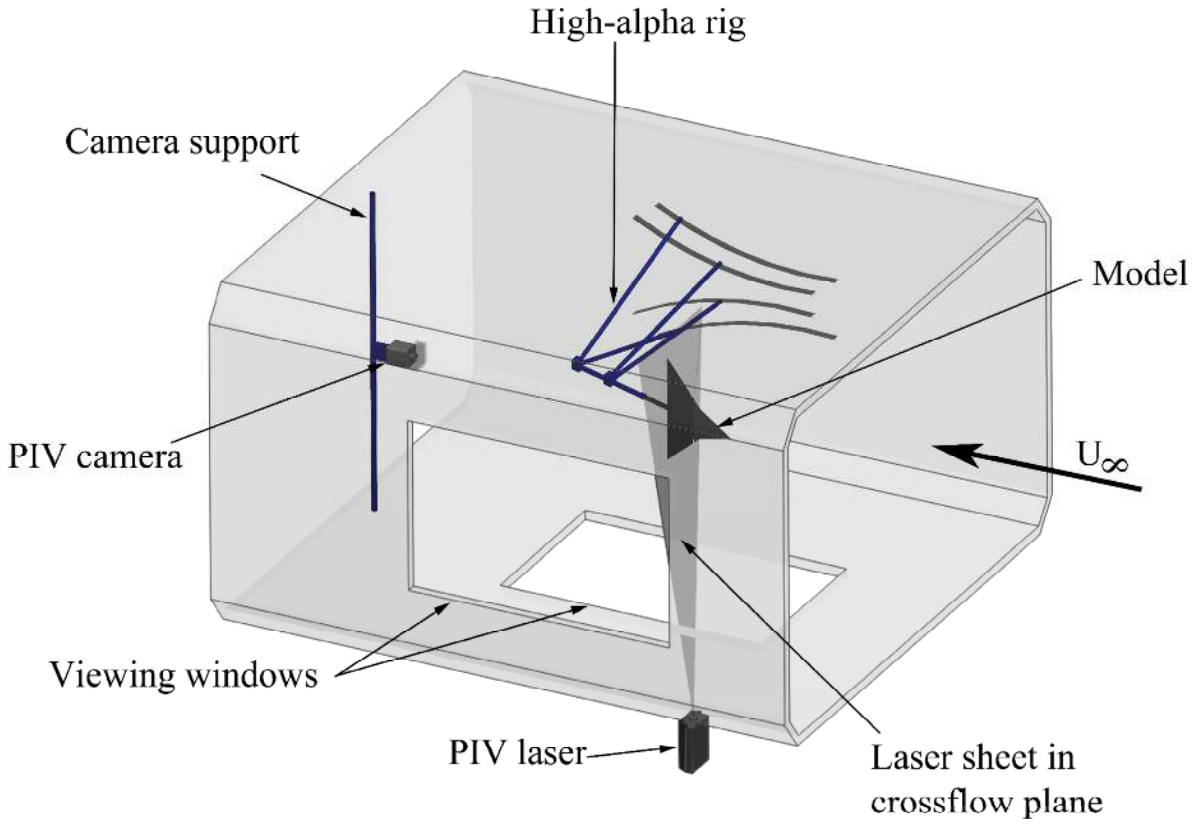

Figure 1. Schematic of experimental setup

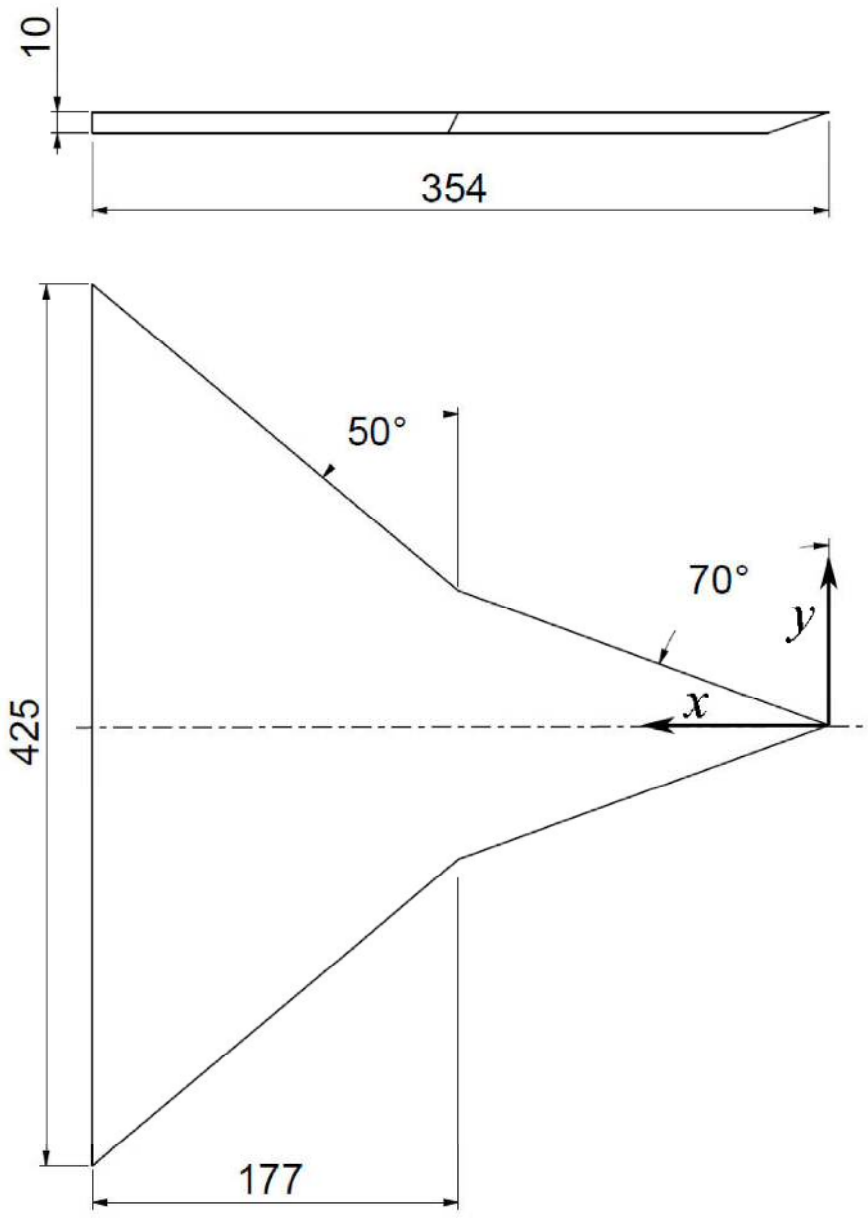

Figure 2. The double delta wing model.

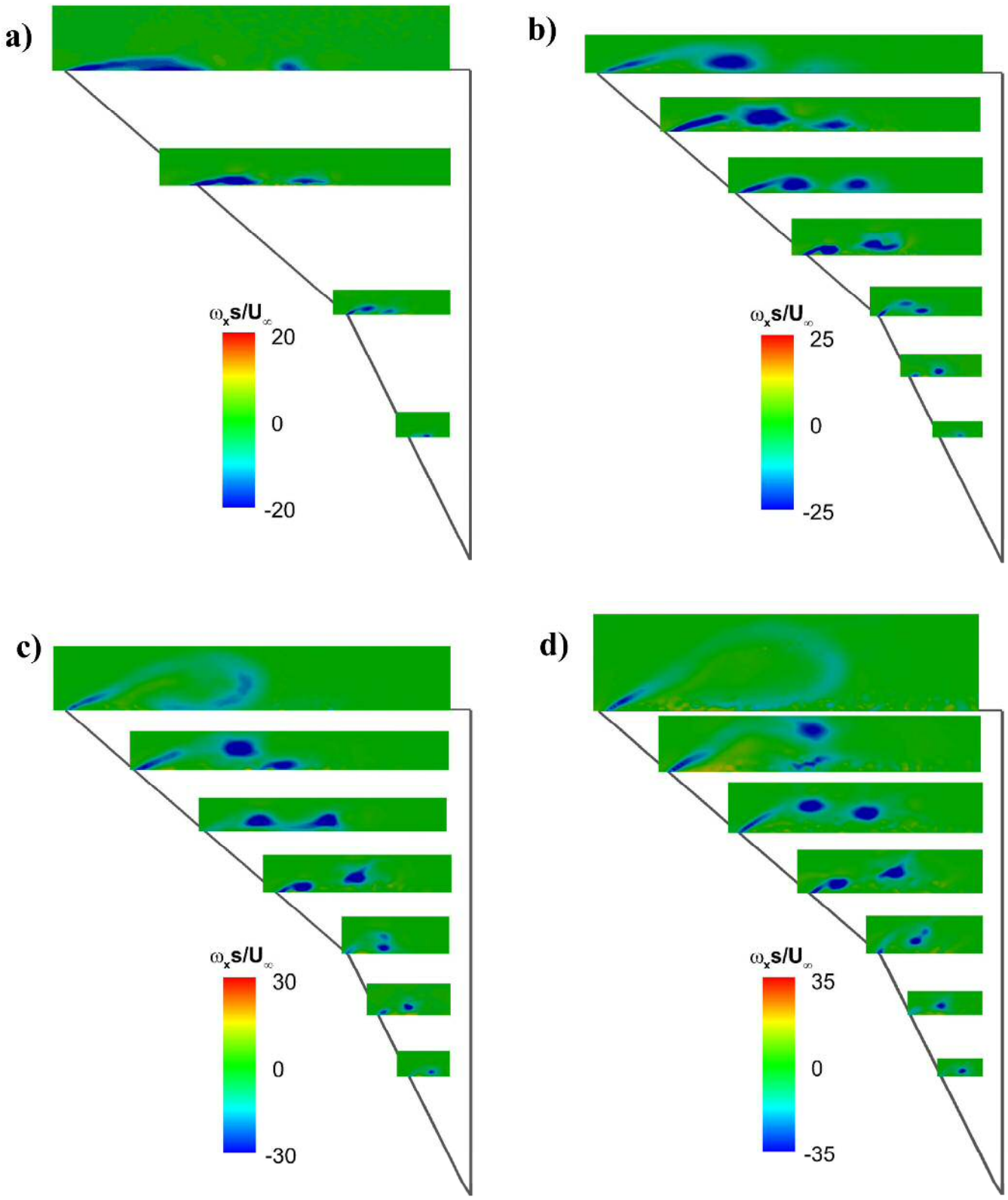

Figure 3. Time-averaged crossflow vorticity patterns over the double delta wing at various chordwise locations at a) α = 4°; b) α = 8°; c) α = 12°; d) α = 16°; e) α = 20°; f) α = 24°; g) α = 28°; h) α = 32°. The chordwise locations are *x/c* = 0.25, 0.375, 0.50, 0.625, 0.75, 0.875, and 1.00. For α = 4° and α = 32°, the locations are *x/c* = 0.25, 0.50, 0.75, and 1.00.

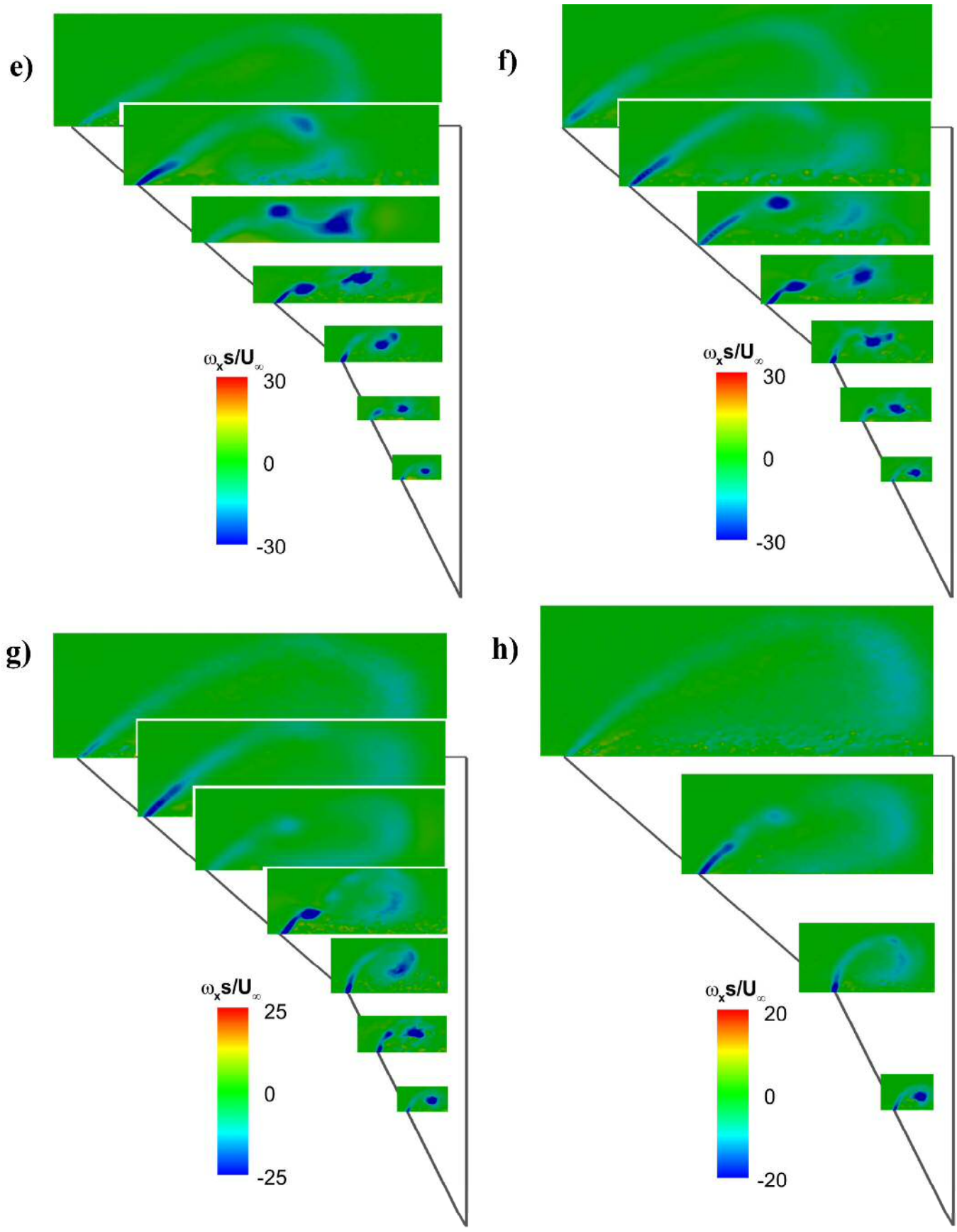

Figure 3. (Continued)

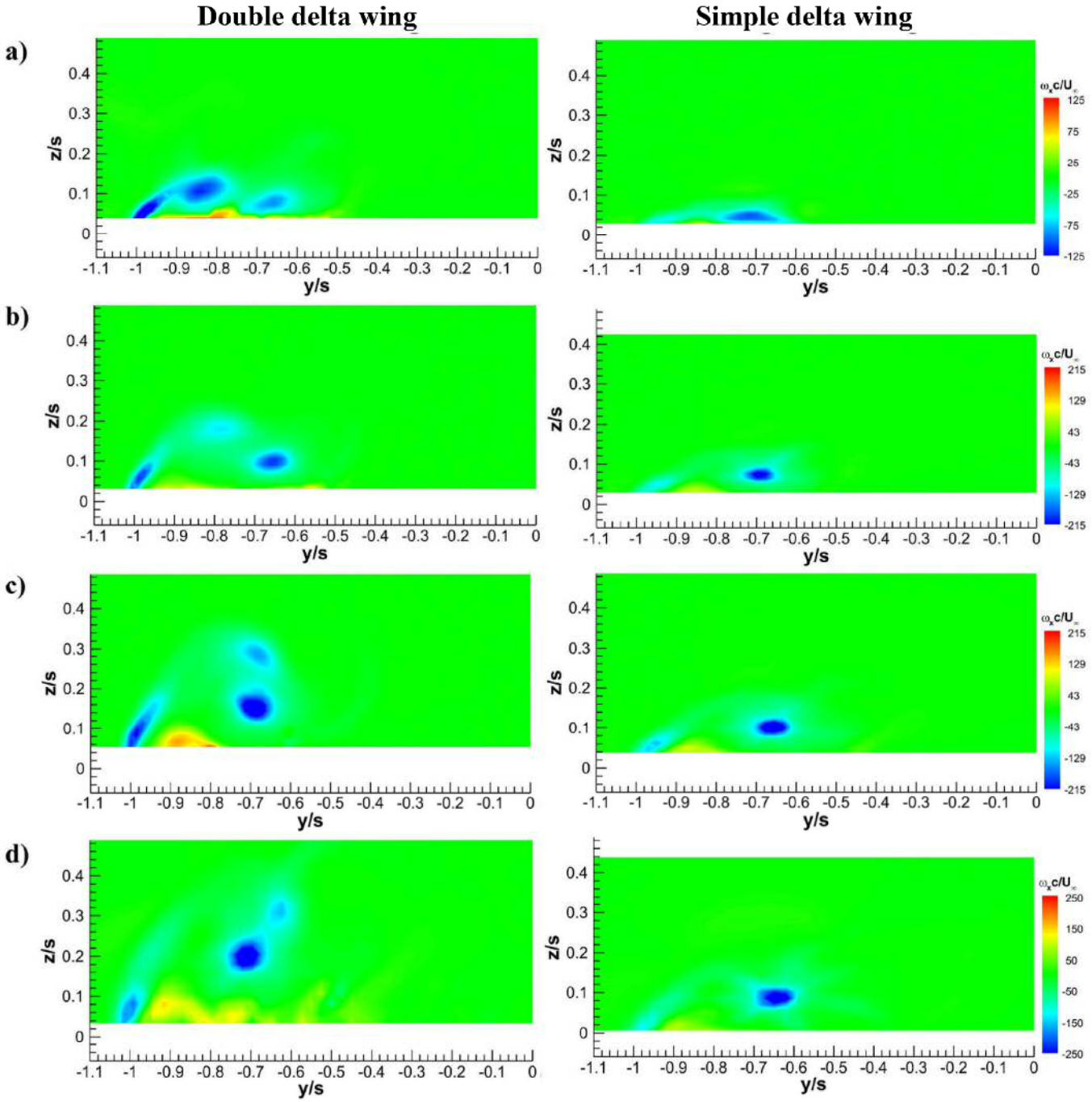

Figure 4. Time-averaged crossflow vorticity patterns over the double delta wing and the simple delta wing at *x/c* = 0.5. a) α = 4°; b) α = 8°; c) α = 12°; d) α = 16°; e) α = 20°; f) α = 24°; g) α = 28°; h) α = 32°.

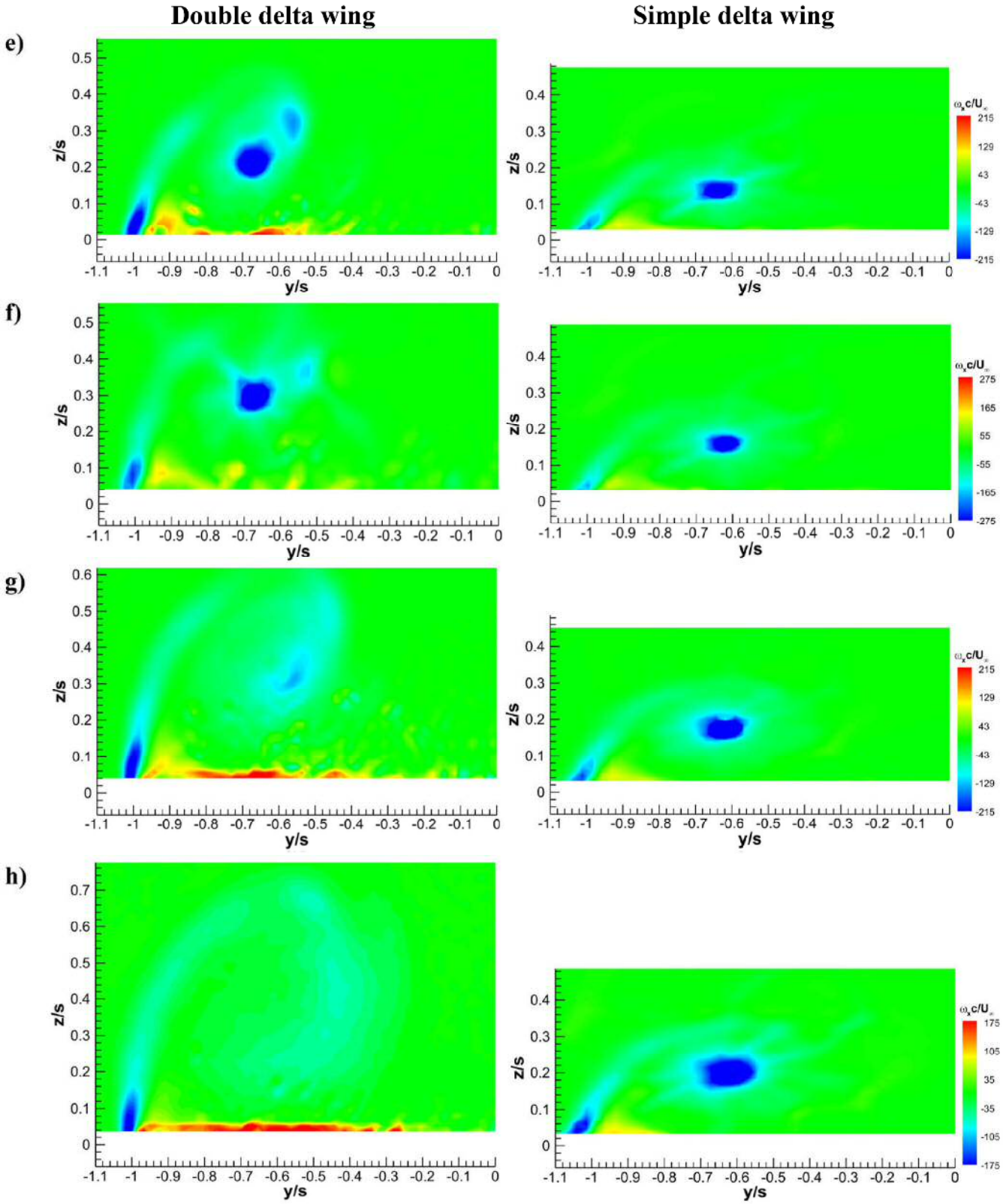

Figure 4. (Continued)

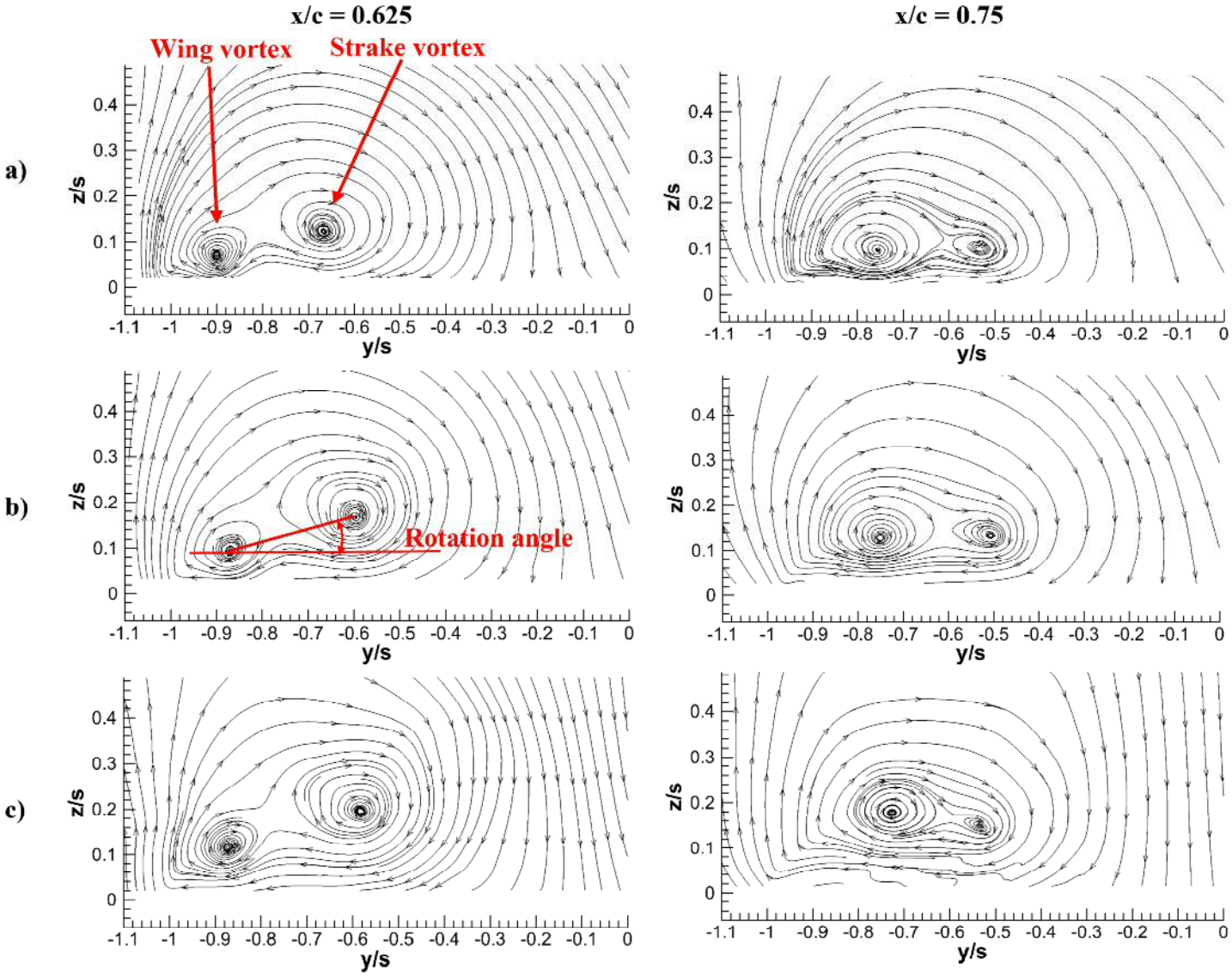

Figure 5. Crossflow streamline patterns over the double delta wing at *x/c* = 0.625 and *x/c* = 0.75. a) α = 8˚; b) α = 12˚; c) α = 16˚; d) α = 20˚; e) α = 24˚; f) α = 28˚.

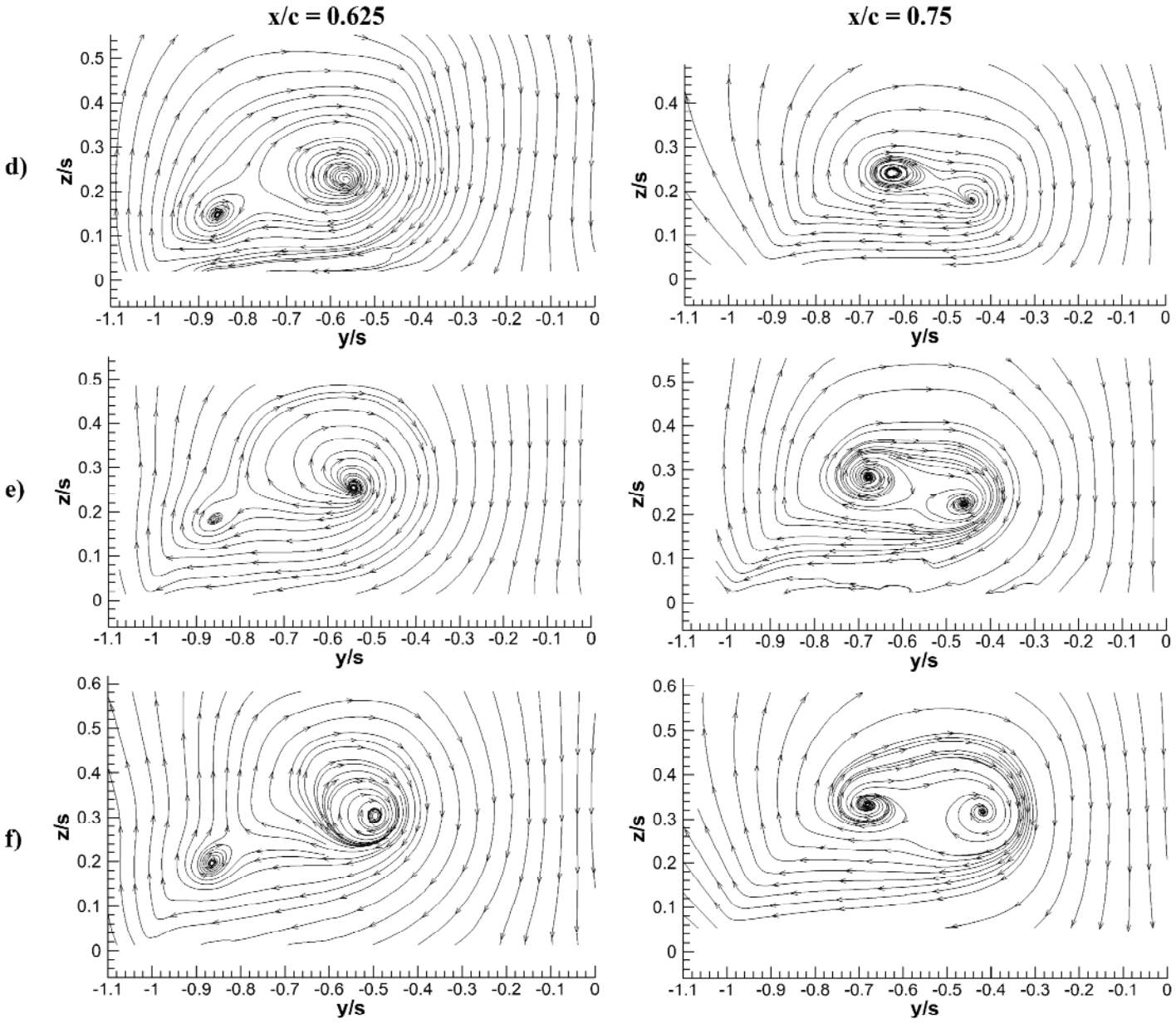

Figure 5. (Continued)

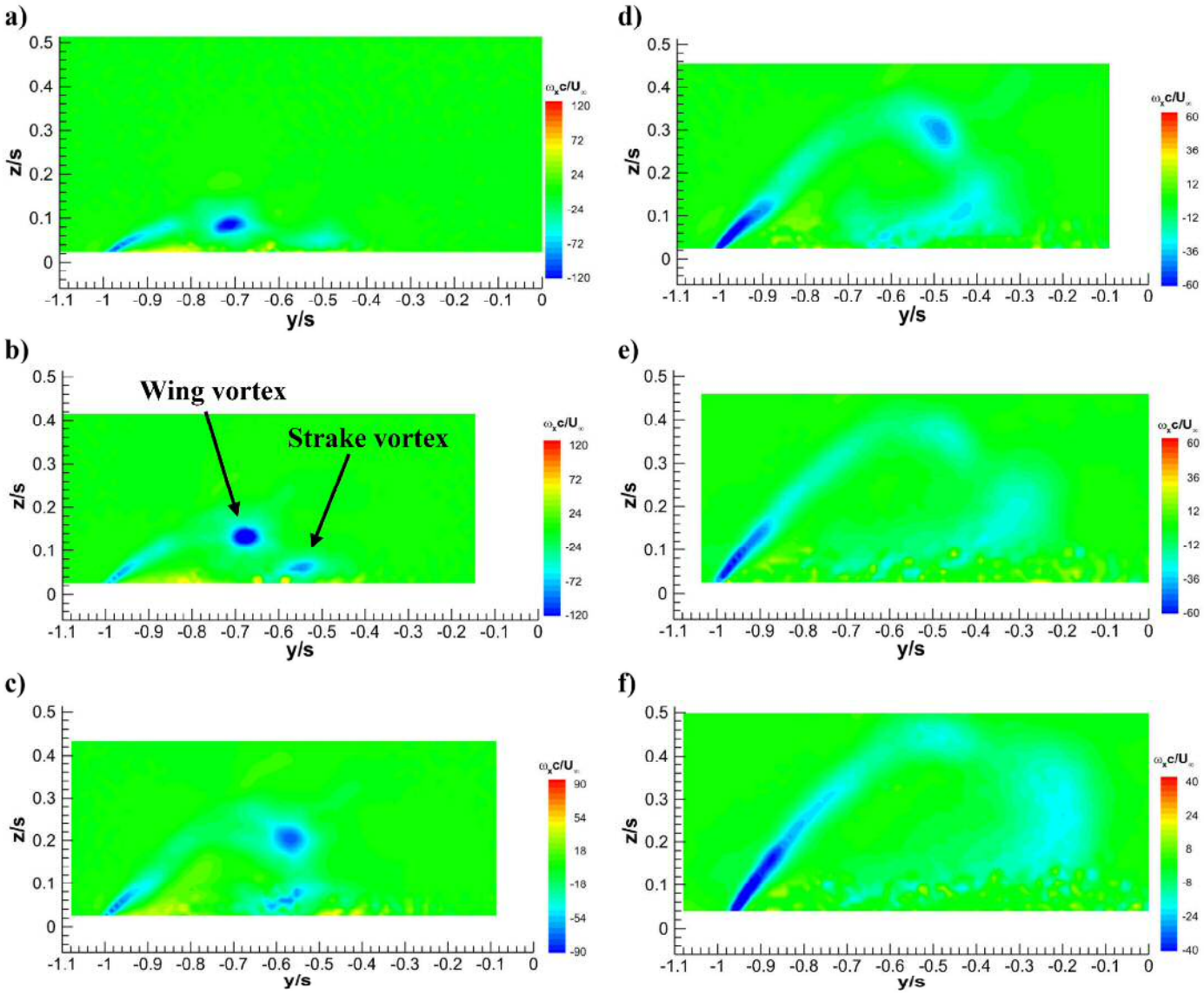

Figure 6. Time-averaged crossflow vorticity patterns over the double delta wing at *x/c* = 0.875. a) α = 8°; b) α = 12°; c) α = 16°; d) α = 20°; e) α = 24°; f) α = 28°.

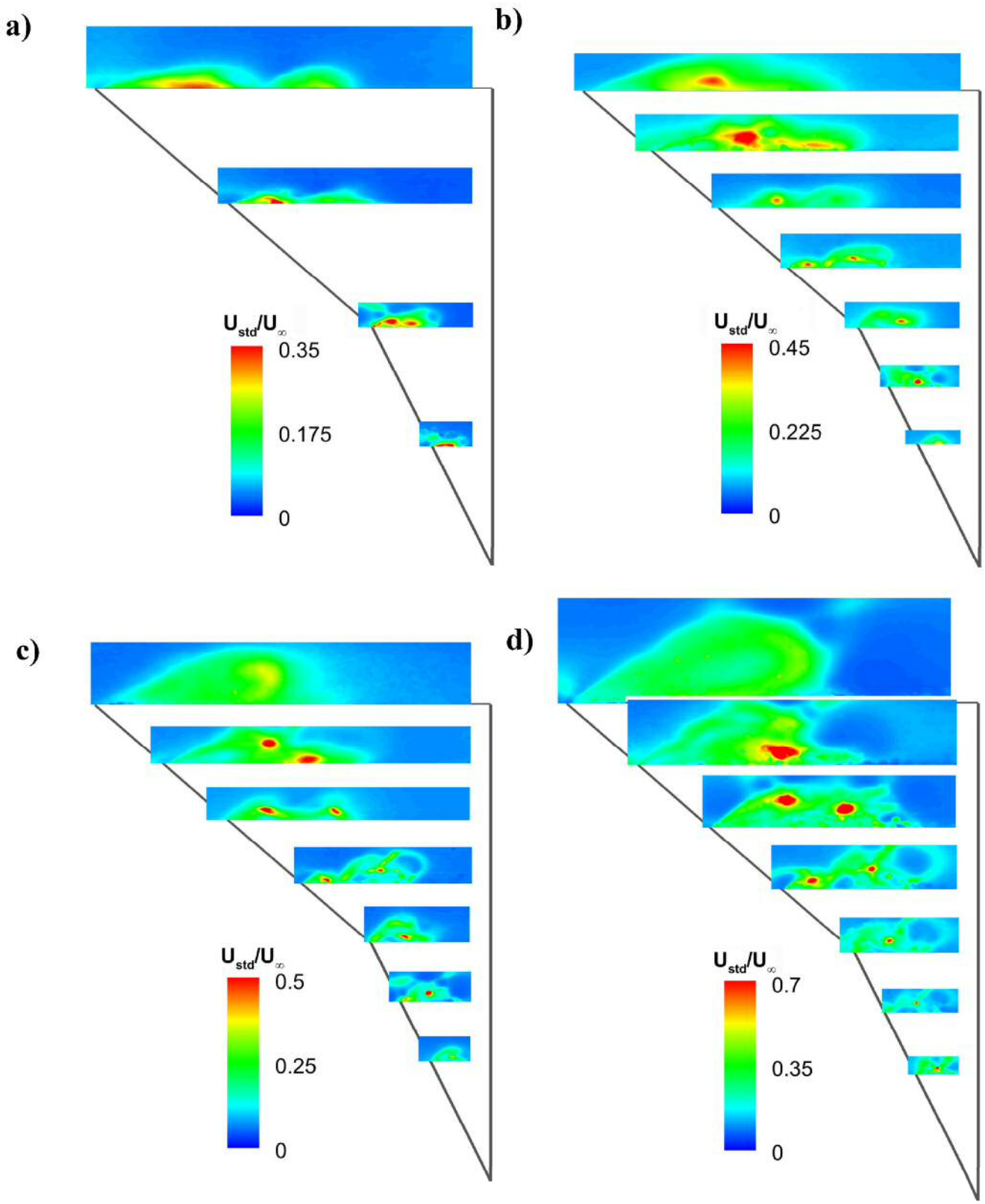

Figure 7. Standard deviation of crossflow velocity fluctuations over the double delta wing at various chordwise locations for a) α = 4˚; b) α = 8˚; c) α = 12˚; d) α = 16˚; e) α = 20˚; f) α = 24˚; g) α = 28˚; h) α = 32˚. The chordwise locations are *x/c* = 0.25, 0.375, 0.50, 0.625, 0.75, 0.875, and 1.00. For α = 4° and α = 32°, the locations are *x/c* = 0.25, 0.50, 0.75, and 1.00.

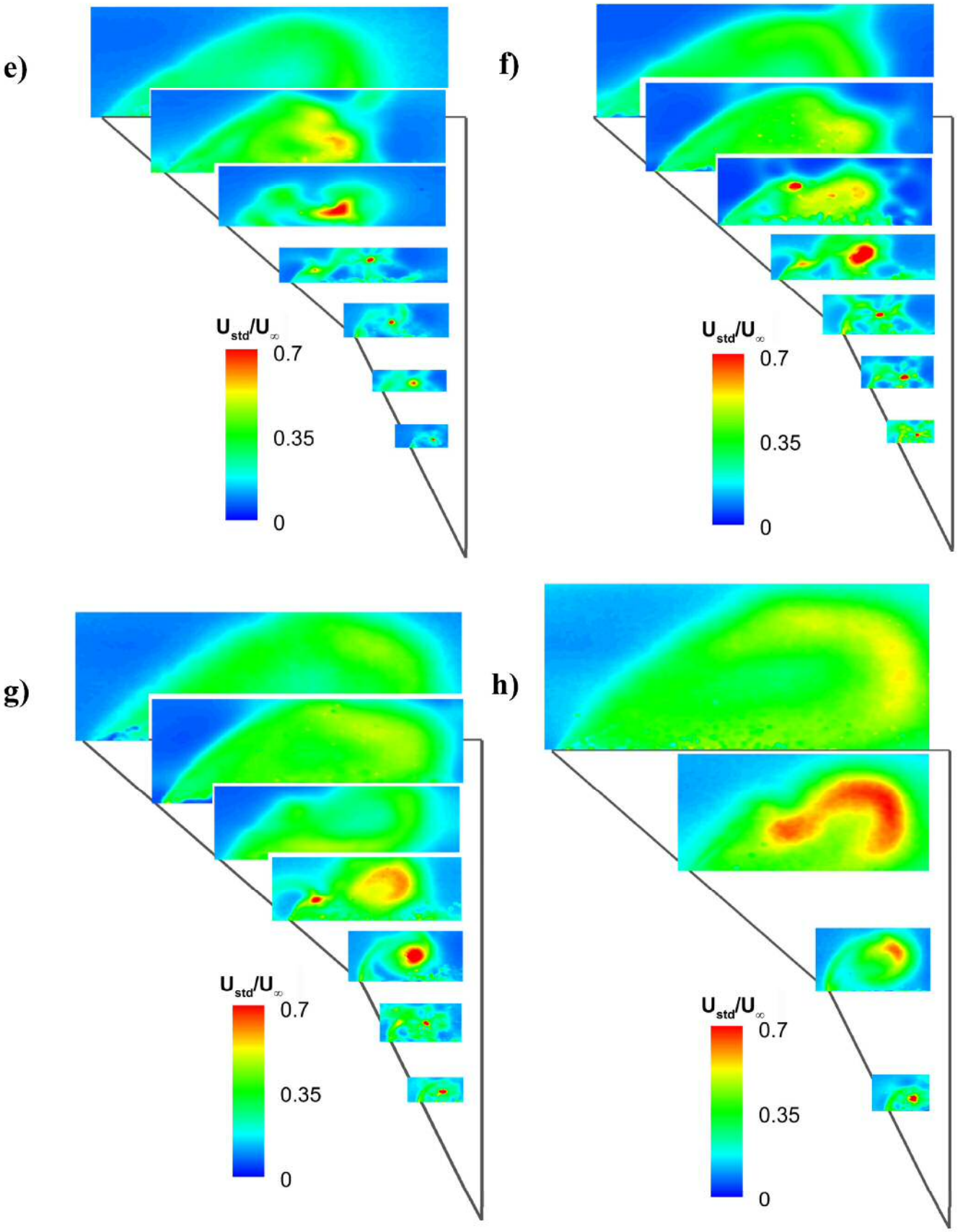

Figure 7. (Continued)

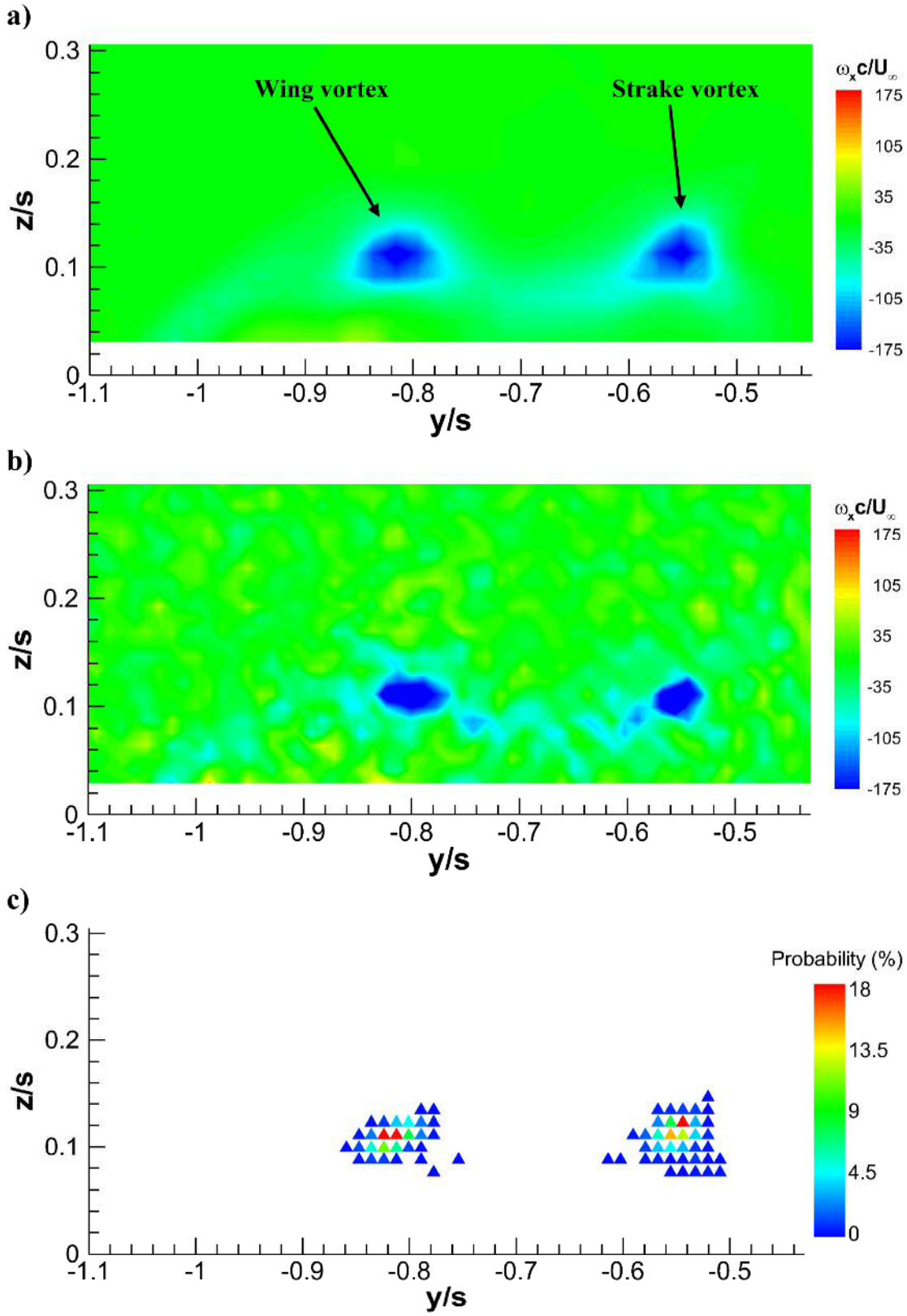

Figure 8. a) Time-averaged crossflow vorticity, b) instantaneous vorticity, and c) probability of instantaneous vortex locations in a crossflow plane over the double delta wing at α = 12° and *x/c* = 0.75.

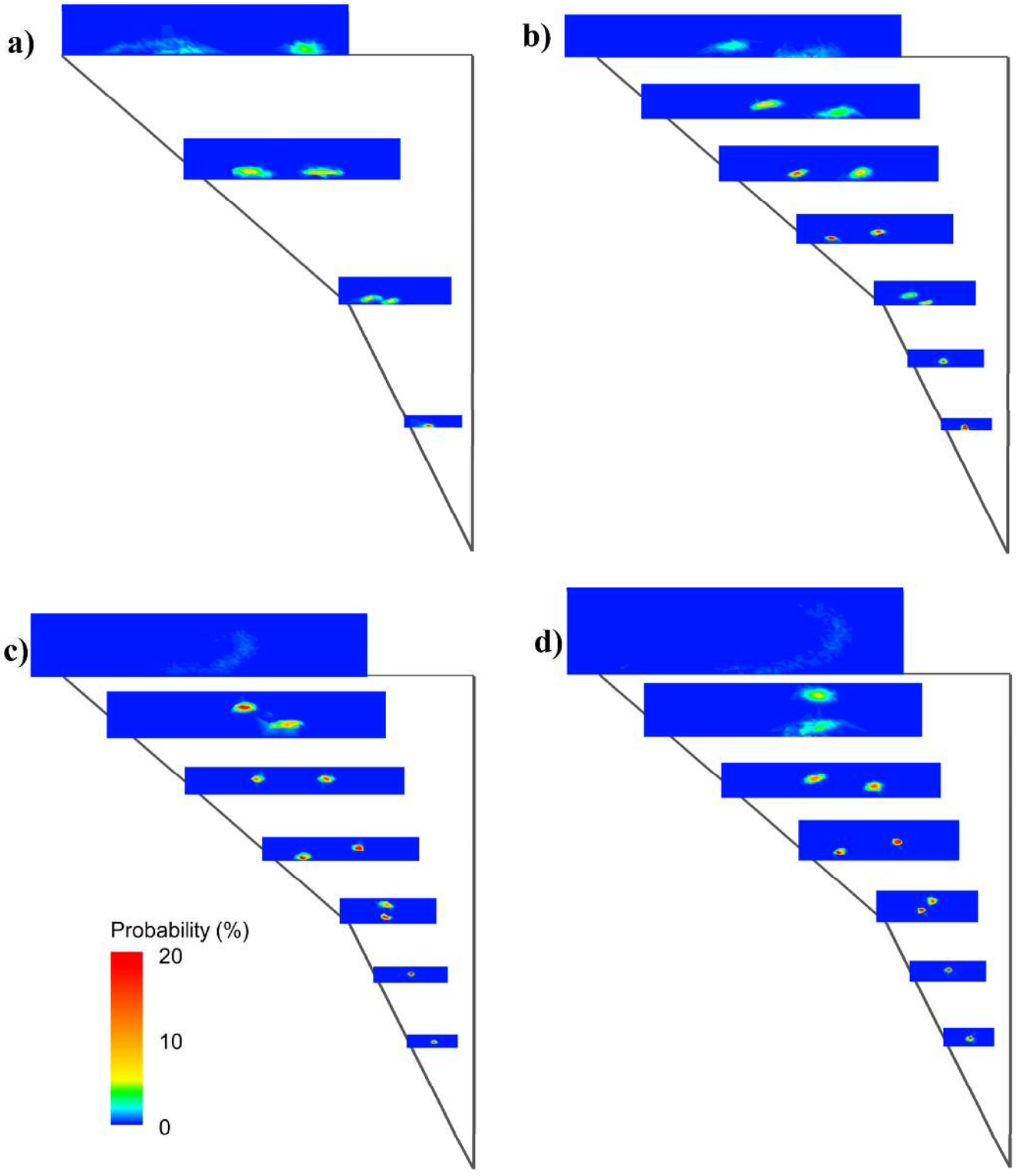

Figure 9. Probability of instantaneous vortex locations over the double delta wing at various chordwise locations for a) α = 4˚; b) α = 8˚; c) α = 12˚; d) α = 16˚; e) α = 20˚; f) α = 24˚; g) α = 28˚; h) α = 32˚. The chordwise locations are *x/c* = 0.25, 0.375, 0.50, 0.625, 0.75, 0.875, and 1.00. For α = 4° and α = 32°, the locations are *x/c* = 0.25, 0.50, 0.75, and 1.00.

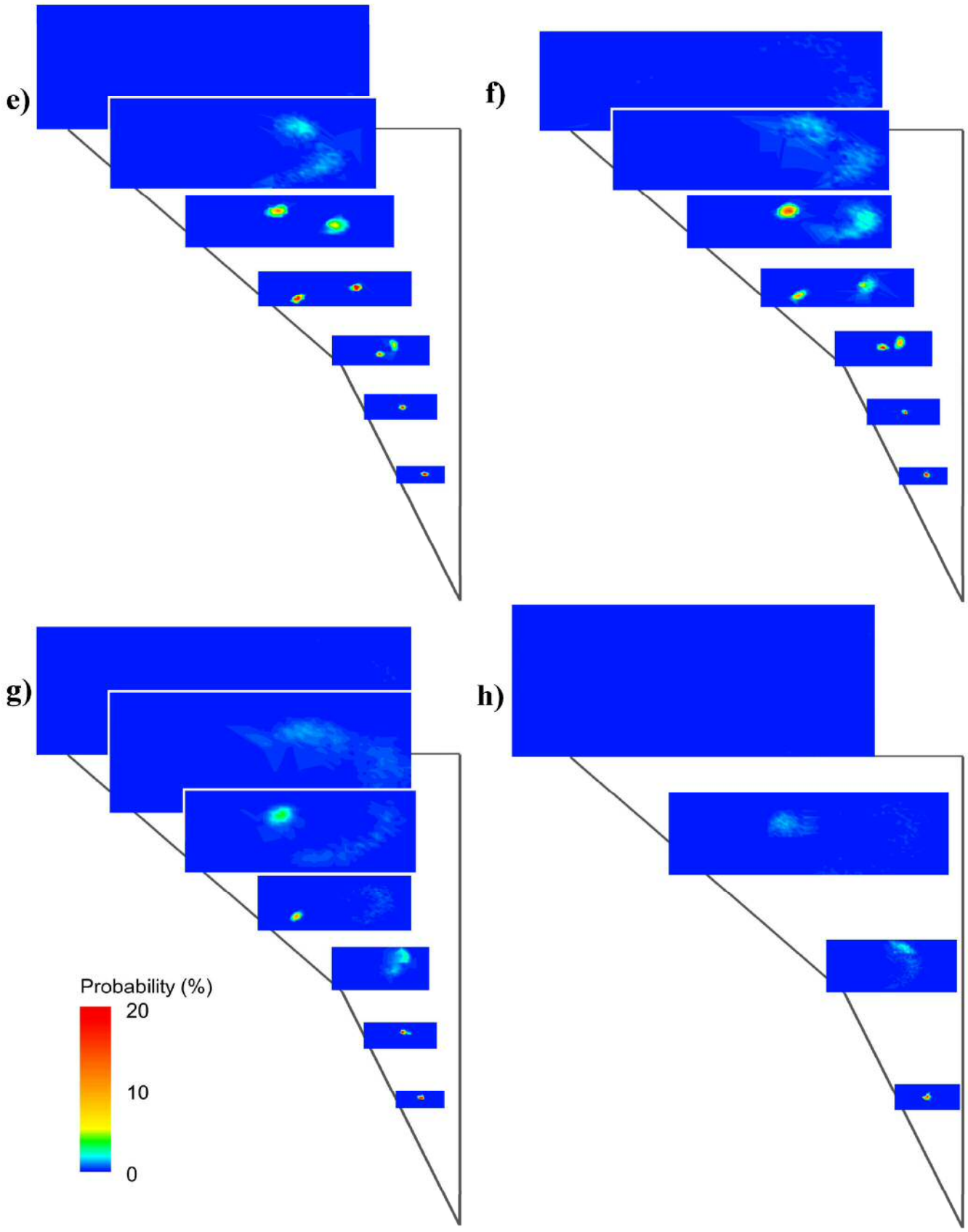

Figure 9. (Continued)

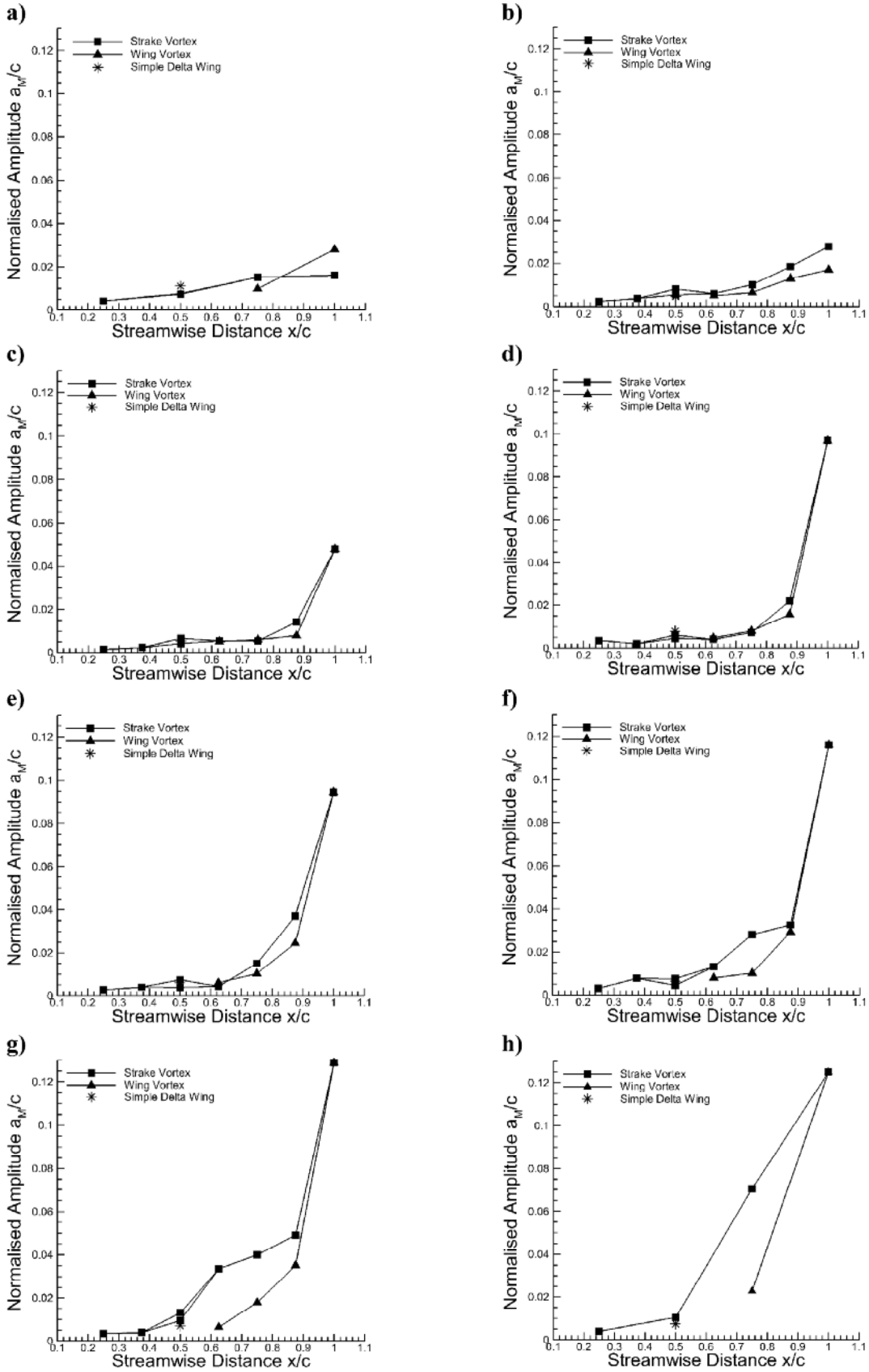

Figure 10. Variation of vortex meandering amplitude as a function of streamwise distance *x/c* for a) α = 4°; b) α = 8°; c) α = 12°; d) α = 16°; e) α = 20°; f) α = 24°; g) α = 28°; h) α = 32°.

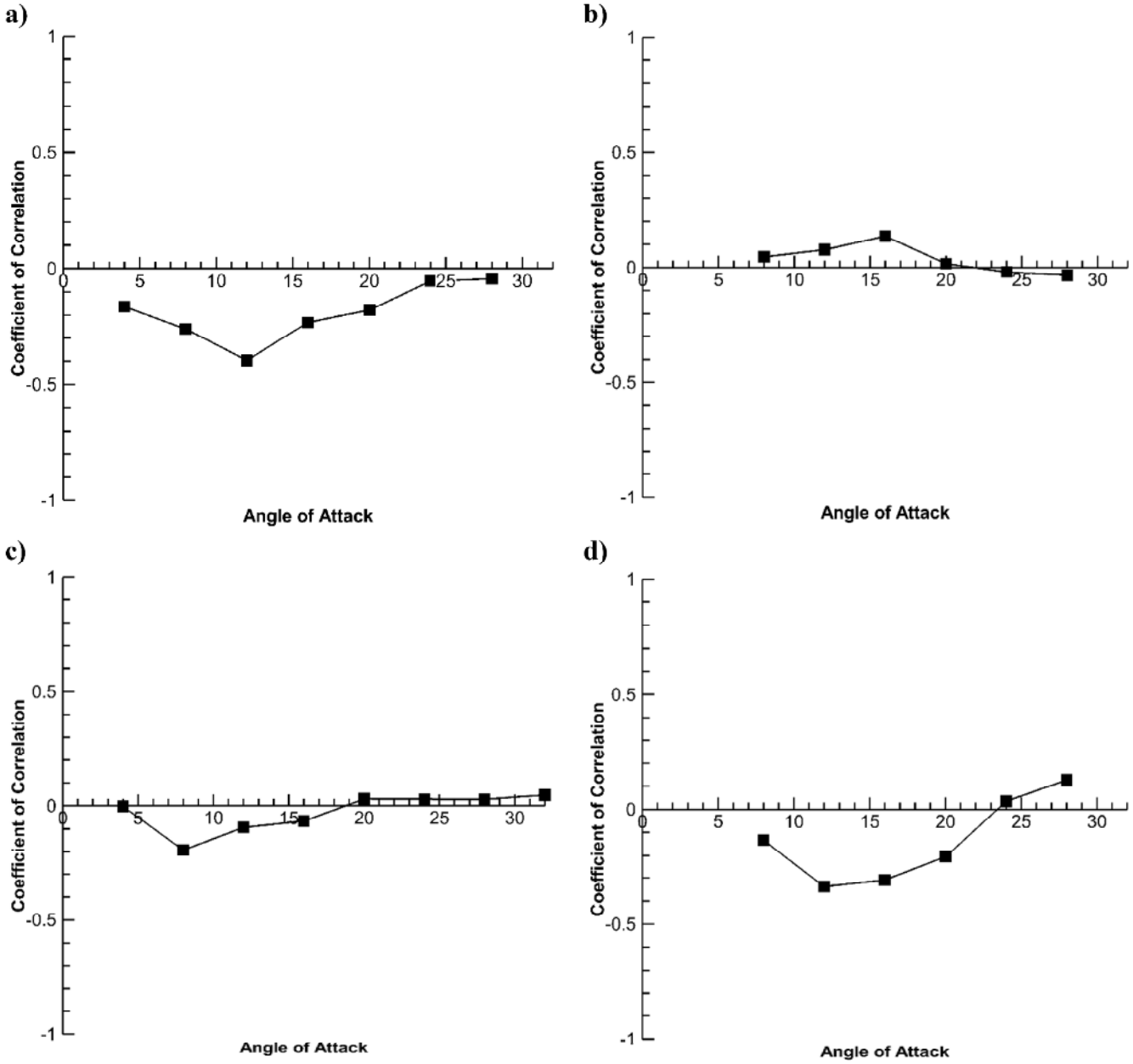

Figure 11. Correlation coefficients between locations of the instantaneous vortices in crossflow planes over the double delta wing at a) *x/c* = 0.5; b) *x/c* = 0.625; c) *x/c* = 0.75; d) *x/c* = 0.875.

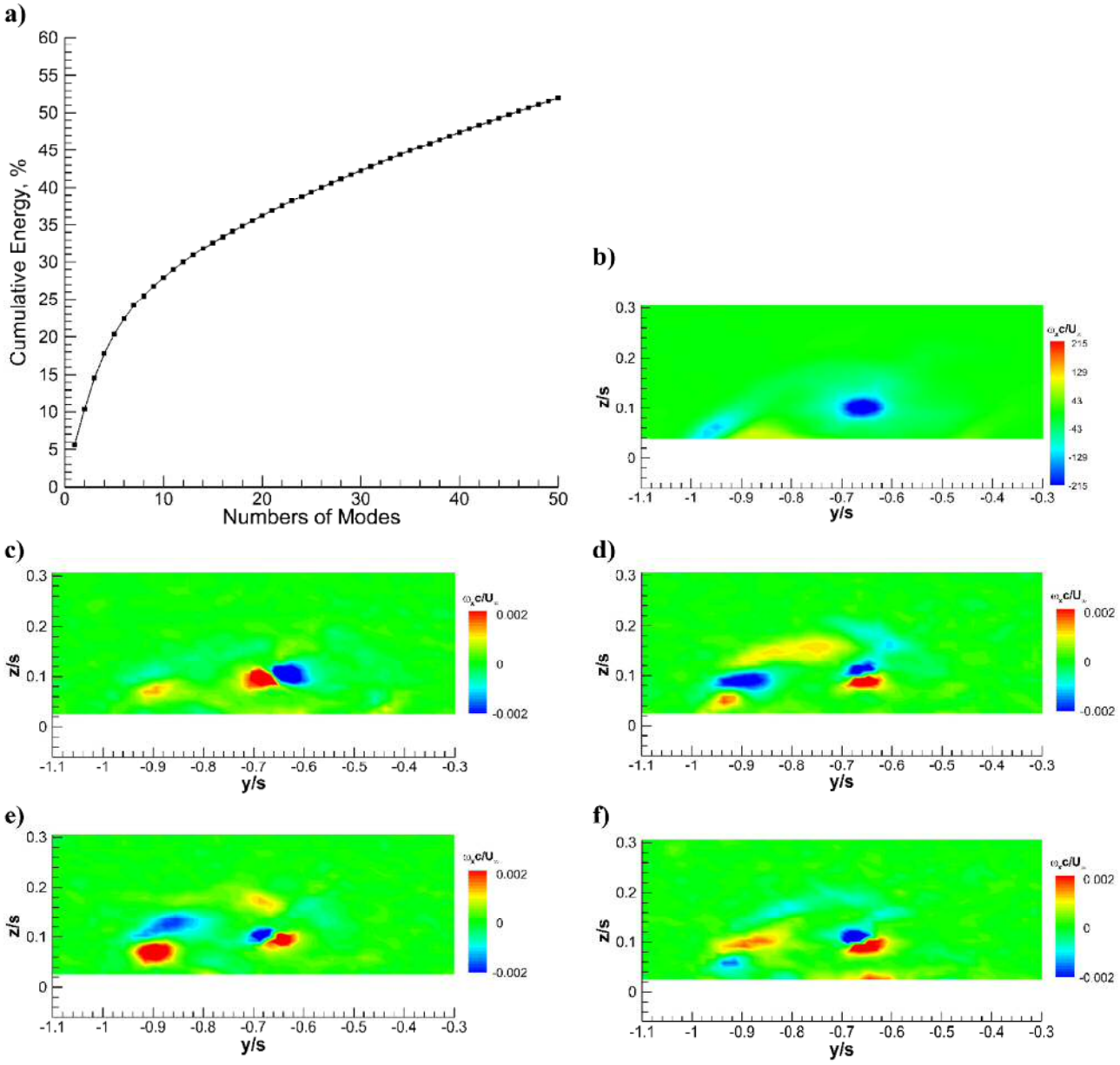

Figure 12. (a) Cumulative energy distribution, (b) time-averaged vorticity field, (c)-(f) flow structures of the 1st, 2nd, 3rd and 4th dominant modes in a crossflow plane over the simple delta wing at *x/c* = 0.5 and α = 12°.

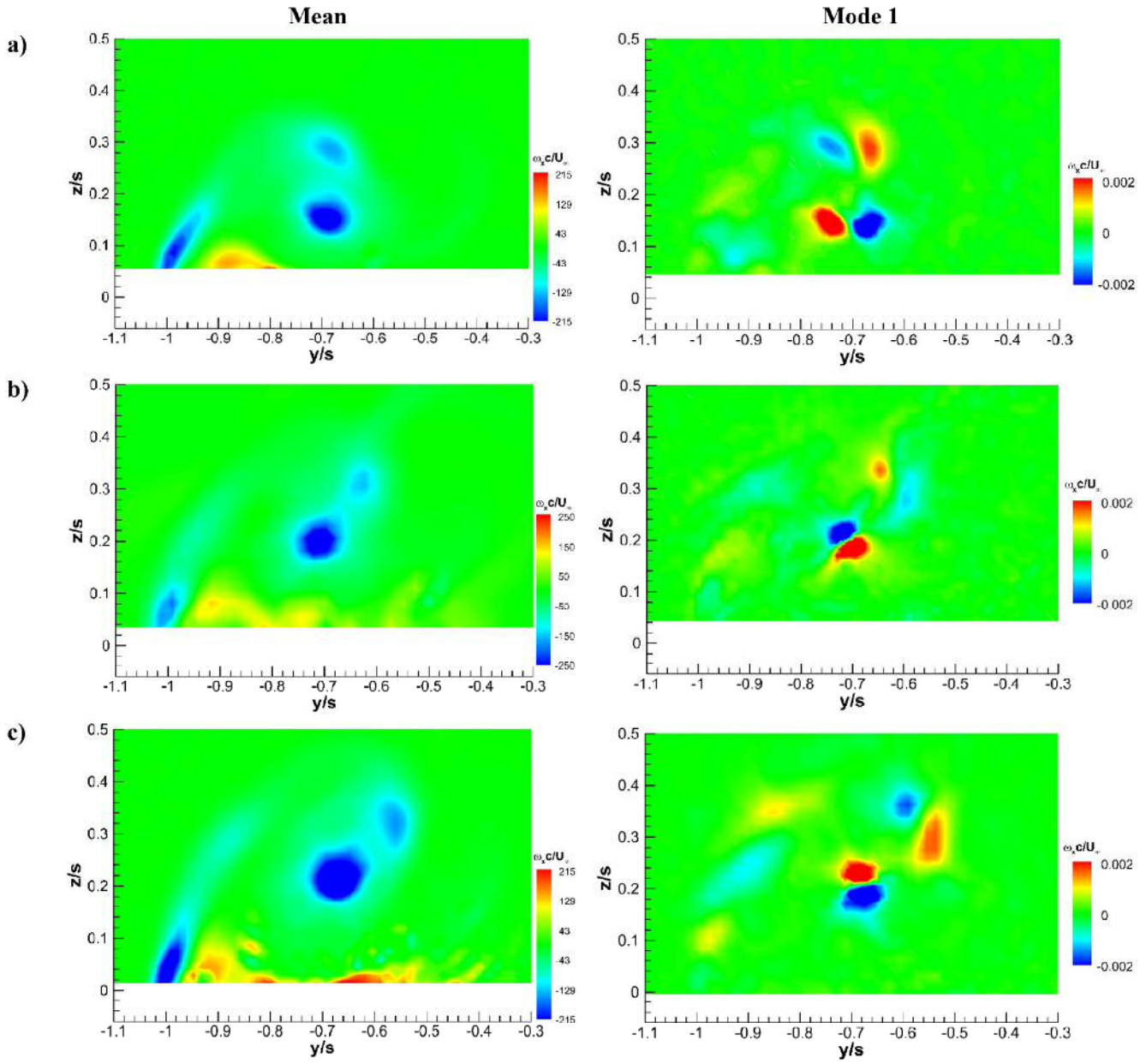

Figure 13. Time-averaged vorticity fields (left column) and flow structures of the first (most energetic) mode in (right column) in a crossflow plane over the double delta wing at *x/c* = 0.5 for a) α = 12˚; b) α = 16˚; c) α = 20˚.

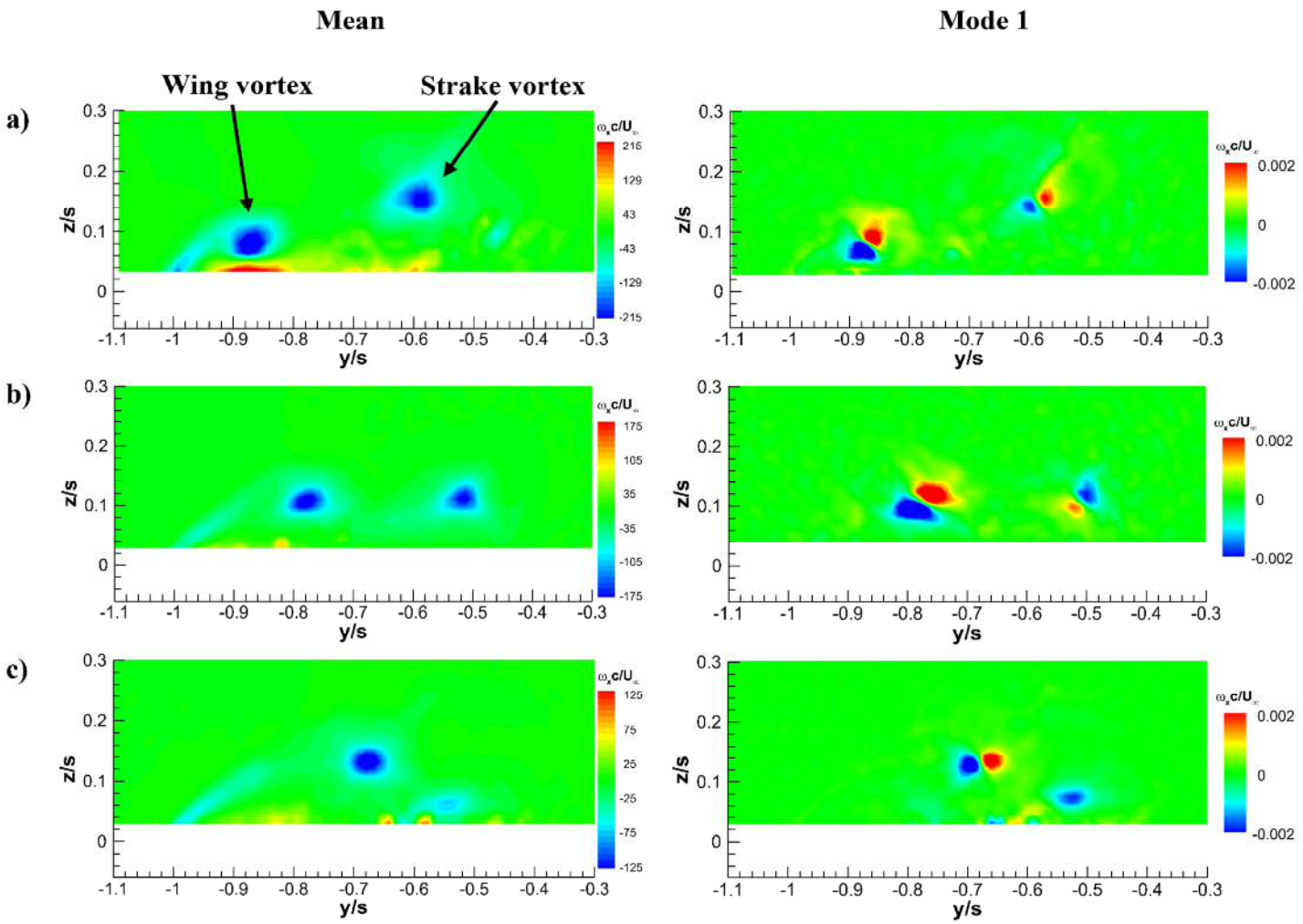

Figure 14. Time-averaged vorticity fields (left column) and flow structures of the first (most energetic) mode in crossflow planes over the double delta wing at α = 12˚, a) *x/c* = 0.625; b) *x/c* = 0.75; c) *x/c* = 0.875.